# Mechanisms for Spontaneous Gravity Wave Generation within a Dipole Vortex

CHRIS SNYDER

*National Center for Atmospheric Research,* Boulder, Colorado*

RIWAL PLOUGONVEN

*Laboratoire de Météorologie Dynamique, IPSL, Ecole Normale Supérieure, Paris, France*

DAVID J. MURAKI

*Department of Mathematics, Simon Fraser University, Vancouver, British Columbia, Canada*

(Manuscript received 16 March 2009, in final form 26 May 2009)

ABSTRACT

Previous simulations of dipole vortices propagating through rotating, stratified fluid have revealed small-scale inertia–gravity waves that are embedded within the dipole near its leading edge and are approximately stationary relative to the dipole. The mechanism by which these waves are generated is investigated, beginning from the observation that the dipole can be reasonably approximated by a balanced quasigeostrophic (QG) solution. The deviations from the QG solution (including the waves) then satisfy linear equations that come from linearization of the governing equations about the QG dipole and are forced by the residual tendency of the QG dipole (i.e., the difference between the time tendency of the QG solution and that of the full primitive equations initialized with the QG fields). The waves do not appear to be generated by an instability of the balanced dipole, as homogeneous solutions of the linear equations amplify little over the time scale for which the linear equations are valid. Linear solutions forced by the residual tendency capture the scale, location, and pattern of the inertia–gravity waves, although they overpredict the wave amplitude by a factor of 2. There is thus strong evidence that the waves are generated as a forced linear response to the balanced flow. The relation to and differences from other theories for wave generation by balanced flows, including those of Lighthill and Ford et al., are discussed.

## 1. Introduction

Snyder et al. (2007, hereafter SMPZ) performed numerical simulations of a dipole vortex in rotating, stratified fluid having uniform potential vorticity and small Rossby number $R = U/fL$, where $U$ and $L$ are velocity and length scales for the dipole and $f$ is twice the rotation rate. The simulations revealed smaller-scale inertia–gravity waves embedded within and stationary with respect to the dipole vortex. These waves appear to be an inherent part of the dipole solution, as they are insensitive to initial conditions and persist in a nearly steady state for many tens of inertial periods. Similar waves have also been found in other dipole simulations, which differ in their numerical techniques and in the details of the dipole vortex (Viúdez 2007, 2008; Wang et al. 2009). The present paper investigates the source mechanism for these inertia–gravity waves.

These waves are of interest as an example of gravity wave generation by a balanced flow.[1] Other simple flows where wave generation occurs include frontogenesis (Snyder et al. 1993; Reeder and Griffiths 1996), elliptical vortices (Ford 1994a), plane waves of potential vorticity in shear (Vanneste and Yavneh 2004), and evolving baroclinic waves (Zhang 2004). The dipole is an especially

* The National Center for Atmospheric Research is sponsored by the National Science Foundation.

*Corresponding author address:* C. Snyder, NCAR, P.O. Box 3000, Boulder, CO 80307–3000.
E-mail: chriss@ucar.edu

[1] We define "balanced flow" or "balanced motion" to be the solution of any approximate governing-equation set for rotating, stratified fluid that filters inertia–gravity waves, in the sense that the equation set supports only slow modal solutions when linearized about a state of rest. Quasigeostrophic flow is an example.

DOI: 10.1175/2009JAS3147.1

useful example, since the characteristics of the balanced flow and the embedded waves are qualitatively similar to those found near the tropopause in baroclinic waves in both observations (Guest et al. 2000; Plougonven et al. 2003) and numerical simulations (Plougonven and Snyder 2007), while the simplified dynamics and time evolution of the dipole facilitate analysis of the source mechanism for the waves.

We consider two possible source mechanisms. The first is an instability of the balanced dipole that would involve inertia–gravity waves, perhaps akin to other instabilities that couple balanced motions and gravity waves (Sakai 1989; Ford 1994a; Plougonven et al. 2005 and references). A second possibility, which we will discuss in greater detail in section 2, is that the waves are a linear forced response to the balanced flow.

Alternative proposals for understanding the wave generation in the dipole include the ''hybrid vortex-wave structure'' of McIntyre (2009). This interpretation emphasizes the nonlinear back reaction of the waves at finite amplitude on the balanced flow. In addition, Viúdez (2008) has analyzed the terms contributing to the vertical velocity in simulations of a dipole vortex similar to those of SMPZ and emphasizes the role of the material rate of change of the horizontal ageostrophic vorticity. This analysis, however, is not a comprehensive dynamical description of the wave generation because it considers only one of the three scalar evolution equations required to describe anelastic hydrostatic flow.

The possibility that the waves arise as a linear forced response to the balanced dipole is broadly analogous to the production by vortical motion of sound (Lighthill 1952) or of gravity waves in shallow water flows (Ford 1994b; Ford et al. 2000). But the inertia–gravity waves found by SMPZ and others differ in two important aspects from the predictions of the Lighthill–Ford theory: they are of smaller scale than the dipole rather than larger scale and they are confined within the dipole rather than appearing in the far field. One goal of the present paper is to clarify the relationship between the Lighthill–Ford theory and the waves found by SMPZ.

Many previous studies write the governing equations in terms of the normal modes for an atmosphere at rest and distinguish slow balanced flow from inertia–gravity waves based on the separation of time scales that obtains when $R$ is small. Wave generation then occurs because the frequency spectrum of the balanced flow in general is not compact but has a weak high-frequency tail that overlaps the frequency range of freely propagating gravity waves (Errico 1982; Warn 1997; Saujani and Shepherd 2002). Balanced motion necessarily excites waves in that frequency range.

The gravity waves generated by the dipole vortex, in contrast, share the same slow temporal scale as the balanced flow but have smaller spatial scale. We argue that both the projection of the balanced dipole onto small spatial scales and the advection of fluid relative to the dipole are necessary for the wave generation, as they allow motions with large intrinsic or Lagrangian frequencies. In essence, the dipole generates waves much as steady flow over smooth but spatially localized orography in a rotating stratified fluid will always produce some steady inertia–gravity waves.

Our approach to the problem begins from the assumption that the flow can be approximated by a balanced solution. Deviations from the balanced solution are then small over some time interval and simple manipulations of the governing equations, outlined in section 2 and following Snyder et al. (1993), lead to a linear forced equation for the deviations, whose validity depends only the smallness of the deviations. Scale analysis of the dispersion relation for inertia–gravity waves provides qualitative explanations for the characteristics of the SMPZ waves and emphasizes how they differ from Lighthill–Ford theory. Section 3 presents a numerical implementation of the forced linear problem and discusses the time interval for which it is valid. Homogeneous solutions of the linear equations are explored first, in section 4, in order to detect possible instabilities of the dipole. Section 5 then investigates the forced linear solution. This solution reproduces reasonably the spatial pattern of emitted waves in the SMPZ dipole simulations but overestimates their amplitude by roughly a factor of 2. Our results and conclusions are summarized in the final section.

## 2. A linear forced analysis of wave generation

### *a. The linear equation*

Our analysis of inertia–gravity wave generation within the dipole rests on the observation that the waves are weak compared with the dipole's flow. Indeed, the waves have little noticeable signature in potential temperature or horizontal velocity. We also assume that the dipole's evolution can be approximated by the quasi-geostrophic (QG) equations or another balanced equation set that filters inertia–gravity waves, at least over a limited time interval whose length will be assessed in section 3.

Let $\mathbf{s}(x, y, z, t)$ represent the dipole solution from the unapproximated equations, where the components of $\mathbf{s}$ are the primitive dependent variables for the flow. For the compressible Boussinesq model used here and in SMPZ, those variables are the velocity components $(u, v, w)$, the

potential temperature $\theta$, and a scaled Exner function $\phi$. Defining $\tilde{\mathbf{s}}(x, y, z, t)$ to be the approximate balanced solution and $\mathbf{s}' = \mathbf{s} - \tilde{\mathbf{s}}$, our basic assumption is that $\mathbf{s}'$, the deviation from the balanced solution, is small.

We write the unapproximated governing equations as

$$\frac{\partial \mathbf{s}}{\partial t} = N(\mathbf{s}), \tag{1}$$

where $N$ is a nonlinear, partial-differential operator. When $\mathbf{s}'$ is small, the rhs of (1) can be expanded in a Taylor series to yield

$$N(\tilde{\mathbf{s}} + \mathbf{s}') = N(\tilde{\mathbf{s}}) + L(\mathbf{s}'; \tilde{\mathbf{s}}) + O(|\mathbf{s}'|^2), \tag{2}$$

where $L(\cdot\,; \tilde{\mathbf{s}})$ is the linear, partial-differential operator obtained by linearizing $N$ about $\tilde{\mathbf{s}}$. In general, $L$ has nonconstant coefficients that vary in both time and space through their dependence on $\tilde{\mathbf{s}}$ and its derivatives.

Since $\partial \mathbf{s}'/\partial t = N(\mathbf{s}) - \partial \tilde{\mathbf{s}}/\partial t$, deviations from the balanced solution then satisfy, to within $O(|\mathbf{s}'|^2)$,

$$\left(\frac{\partial}{\partial t} - L\right)\mathbf{s}' = N(\tilde{\mathbf{s}}) - \frac{\partial \tilde{\mathbf{s}}}{\partial t}. \tag{3}$$

Thus, $\mathbf{s}'$ evolves according to a linear partial-differential equation with nonconstant coefficients that is forced by a known function of the balanced solution $\tilde{\mathbf{s}}$. We will refer to the forcing as a residual tendency because it is the difference between $N(\tilde{\mathbf{s}})$, the instantaneous time tendency that would be produced if the balanced solution were substituted in the full equations, and $\partial \tilde{\mathbf{s}}/\partial t$, the time tendency of the approximate balanced solution itself.

Equation (3) is clearly valid if $\mathbf{s}'$ is sufficiently small. We leave open the question of just how small $\mathbf{s}'$ must be in terms of external parameters such as $R$. Instead, we use (3) as motivation for the numerical solutions presented in sections 3–5 and simply check its validity a posteriori by comparing against the difference between the full nonlinear solution of (1) and the balanced solution.

Calculating the forcing requires not only the balanced solution $\tilde{\mathbf{s}}$ itself, which is provided by most techniques for potential-vorticity inversion, but also $\partial \tilde{\mathbf{s}}/\partial t$. Indeed, strong cancellation will typically occur between $N(\tilde{\mathbf{s}})$ and $\partial \tilde{\mathbf{s}}/\partial t$, since the latter is an approximation of the former. Balanced solutions whose order of accuracy in an expansion in $R$ is $n$ will yield residual tendency $N(\tilde{\mathbf{s}}) - \partial \tilde{\mathbf{s}}/\partial t$ that is $O(R^n)$ compared to either term individually.

The only approximation required for (3) is neglect of terms that are nonlinear in $\mathbf{s}'$. As originally emphasized by Lighthill (1952) and more recently by McIntyre (2009), this removes any back reaction by the deviations on the original balanced flow and allows $\mathbf{s}'$ to be considered as a response forced by the balanced flow. McIntyre (2009) argues that the wave generation within the dipole is associated with significant back reaction on the balanced flow and thus may not be understood by (3).

Forced, linear equations like (3) have been derived previously. In studies of gravity wave generation by frontogenesis, Ley and Peltier (1978) and Snyder et al. (1993) proceed in the same manner as here but develop equations for the specific case of two-dimensional frontogenesis, with a balanced solution given by the semigeostrophic solution. M. Reeder (2004, unpublished manuscript) has computed the forced solutions numerically and shown them to be excellent approximations to the deviations from the semigeostrophic frontogenesis solution.

An important aspect of equations like (3) is that the operator $L(\cdot; \tilde{\mathbf{s}})$ has nonconstant coefficients, implying that the gravity wave solutions differ from gravity waves in a fluid at rest. Plougonven and Zhang (2007) have derived heuristically, using scale analysis, forced linear equations governing the small-scale component of the flow. They show that advection by the balanced flow should be retained in $L$ if the deviations $\mathbf{s}'$ are of much smaller spatial scale than the balanced motion, as is the case in the dipole and in other simulated and observed inertia–gravity waves associated with fronts and jets. Any waves generated then feel the effects of propagation through a slowly varying medium. Plougonven and Snyder (2005) give an example of the importance of such effects.

Another approach is to manipulate (1) as in Lighthill (1952) or Ford et al. (2000), moving any purely linear terms to the lhs and evaluating the remaining nonlinear terms from an approximate balanced solution. The resulting equation would differ from (3) in its neglect of those terms in the operator $L(\cdot, \tilde{\mathbf{s}})$ that arise from the linearization of nonlinearities such as advection. Reeder and Griffiths (1996) adopt a similar approach, again in the context of wave generation by frontogenesis. They treat nonlinear terms as in Lighthill (1952) and evaluate them as a forcing using the semigeostrophic solution. But because they begin with equations for perturbations to a large-scale frontogenetic flow, the linear operator on the lhs has variable coefficients arising from the large-scale flow and captures some aspects of variations of the medium on the wave propagation.

### b. Discussion

Some important inferences follow immediately from (3). First, unless the rhs of (3) has a very special form, it will have some projection on temporal frequencies and spatial scales corresponding to inertia–gravity waves propagating through a medium defined by the dipole's

flow. Thus, $\mathbf{s}'$ should in general include forced waves, as detailed in Warn (1997) for the generation of fast waves by slow balanced motion.

Second, (3) also admits wave generation through instabilities that couple balanced motions and gravity waves, like those already identified for the shallow-water equations (Ford 1994a) and continuously stratified rotating flows (Plougonven et al. 2005 and references therein). Such instabilities are homogeneous solutions of (3) for steady balanced flows.

Third, $\mathbf{s}'$ will include balanced motions, in the form of higher-order corrections to $\tilde{\mathbf{s}}$, such as might be obtained by an expansion in Rossby number or Froude number. These corrections will in general exhibit secular growth with time and thus will not remain small, as discussed in Warn et al. (1995). Because of this, (3) will be valid only for a limited time interval. We estimate the length of this interval for the dipole in section 3 and show how balanced corrections can grow with time in section 4.

While it is clear that $\mathbf{s}'$ will in general include inertia–gravity waves, the amplitude of those waves remains an open and difficult question. The rhs of (3) shares the spatial and temporal scales of the balanced motion. Thus, when there is scale separation in time or space between waves and balanced motions, the projection of the forcing onto waves will be weak and the wave response will be much smaller than order-of-magnitude consideration of the rhs of (3) would imply. For example, Medvedev and Gavrilov (1995) arrive at a forced linear equation similar to (3) through a multiple time-scale expansion, yet detailed analysis of the solutions shows that there is zero projection of the slow forcing onto fast waves at the order of truncation they consider. Indeed, because of the weak projection of the forcing onto waves when $R$ is small, the wave response may be exponentially small in $R$ (Warn 1997; Saujani and Shepherd 2002; Vanneste 2008), so that asymptotic expansion of (1) for $R \ll 1$ will not include the spontaneously generated waves at any algebraic power of $R$.

Leaving aside the question of the wave amplitude, scale analysis provides several constraints on other characteristics of spontaneously generated waves. Consider the nondimensional dispersion relation for inertia–gravity waves in a slowly varying, background flow $(u, v, 0)$:

$$R^2(\omega - ku - lv)^2 = \frac{1 + B^2(k^2 + l^2)}{m^2}. \qquad (4)$$

Here, $(k, l, m)$ and $\omega$ are the local wave vector and frequency, respectively, $B = NH/fL$ is the Burger number, and the nondimensionalization employs the velocity, length, and height scales ($U$, $L$, and $H$, respectively) of the balanced flow together with the advective time scale $L/U$. In the absence of a background flow, the wave frequency is necessarily $O(R^{-1})$ or larger.

For the dipole, $R$ is small and $B = O(1)$. At least one of $\omega$ and $(k, l)$ must then be $O(R^{-1})$ to satisfy (4). Thus, two classes of waves are possible, either high frequency compared to the balanced motion or of much smaller horizontal scale than the balanced motion. The waves with small horizontal scale must have small vertical scale as well to maintain a wave–vector slope that is consistent with the (near-inertial) intrinsic frequency. The projection of the residual tendency onto either class of wave will be weak and determining the wave amplitude becomes a subtle question, as already noted.

The dipole is nearly steady in the comoving frame and so the residual tendency that forces (3) will be almost steady, with even less excitation of frequencies $\omega \sim R^{-1}$ than a typical QG flow. Thus, the dispersion relation (4) alone predicts that any waves emitted by the dipole should have small horizontal and vertical scale, with $k$, $m \sim R^{-1}$, and should be approximately stationary with respect to the dipole. Each of these characteristics is observed in the SMPZ simulations.

The possibility of small-scale waves whose absolute frequency is comparable to or smaller than that of the balanced flow [i.e., $\omega = O(1)$] depends on the presence of the background flow $(u, v, 0)$. Motions with sufficiently small scales in the direction of the flow can then have intrinsic frequencies that are large—larger than $f$ and in the range of inertia–gravity waves. Mathematically, there may be a nonzero response to steady forcing through the term $L(\mathbf{s}', \tilde{\mathbf{s}})$ in (3) even though $\partial\mathbf{s}'/\partial t$ is small or zero. This is analogous to the forcing of steady waves by fixed topography and a steady background wind. Methods based purely on a separation of time scales between balanced motions and waves will overlook the class of small-scale waves, as will approaches that, following Lighthill (1952) or Ford et al. (2000), retain on the lhs of (3) only those terms appropriate for inertia–gravity waves in a rotating fluid at rest.

The situation is different for rotating shallow-water flow. In that case, the dispersion relation for inertia–gravity waves is

$$R^2(\omega - ku - lv)^2 = 1 + (R^2/F^2)(k^2 + l^2),$$

where now $F = U/\sqrt{gH}$ and $H$ is the fluid depth. If $R \ll 1$ and $F \sim R$, then the dispersion relation requires $\omega = O(R^{-1})$ and $k = O(1)$; the waves must be fast compared to the balanced motion but share the same spatial scale. Consistent with this, in this regime Kizner et al. (2008) find steadily propagating dipole solutions for rotating shallow water that, unlike the continuously stratified

dipole, do not exhibit embedded copropagating inertia–gravity waves. When $R = O(1)$ and $F \ll 1$, then waves can have $\omega = O(1)$ as long as $k, l = O(F)$. This is the regime of Ford et al. (2000) in which the waves are long and inherit their Eulerian frequency, which is larger than $f$, from the balanced motion. In both regimes, the background flow makes a negligible contribution to the intrinsic frequency of the waves and thus our conclusions are the same as those of Saujani and Shepherd (2002), who consider the shallow-water dispersion relation without a background flow.

## 3. The forced linear model and its accuracy

In this section, we give the detailed formulation of the forced linear model and assess the time interval over which its solutions are useful.

The simulations of SMPZ are based on the Boussinesq, compressible, nonhydrostatic equations for a uniformly rotating fluid. The governing equations represented schematically in (1) thus have the specific form

$$\frac{\partial \mathbf{v}}{\partial t} = -\mathbf{v}\cdot\nabla\mathbf{v} - f\mathbf{k}\times\mathbf{v} - \nabla\phi + \frac{g\theta}{\theta_0}\mathbf{k}, \tag{5a}$$

$$\frac{\partial \phi}{\partial t} = -\mathbf{v}\cdot\nabla\phi - c_s^2\nabla\cdot\mathbf{v}, \quad \text{and} \tag{5b}$$

$$\frac{\partial \theta}{\partial t} = -\mathbf{v}\cdot\nabla\theta, \tag{5c}$$

where $\phi = c_p\theta_0(p/p_0)^{R/c_p}$, $\theta_0$ is a reference potential temperature, $p_0$ is a reference pressure, $c_s$ is the constant speed of sound, and other notation is conventional. We will abuse terminology slightly by referring to (5) as the primitive equations (PEs). Even though prognostic equations for the vertical velocity $w$ and for $\phi$ are included in (5), the flow is nearly hydrostatic and incompressible for the spatial and temporal scales that characterize the dipole, including the embedded inertia–gravity waves.

Given an approximate, balanced solution with fields $\tilde{\mathbf{v}}$, $\tilde{\theta}$, and $\tilde{\phi}$, which may vary in space and time, (5) can be linearized about that solution to yield the counterpart of (3):

$$\left(\frac{\partial}{\partial t} + \tilde{\mathbf{v}}\cdot\nabla\right)\mathbf{v}' + \mathbf{v}'\cdot\nabla\tilde{\mathbf{v}} + f\mathbf{k}\times\mathbf{v}' + \nabla\phi' - \frac{g\theta'}{\theta_0}\mathbf{k} = (F_u, F_v, F_w), \tag{6a}$$

$$\left(\frac{\partial}{\partial t} + \tilde{\mathbf{v}}\cdot\nabla\right)\phi' + \mathbf{v}'\cdot\nabla\tilde{\phi} + c_s^2\nabla\cdot v = F_\phi, \quad \text{and} \tag{6b}$$

$$\left(\frac{\partial}{\partial t} + \tilde{\mathbf{v}}\cdot\nabla\right)\theta' + \mathbf{v}'\cdot\nabla\tilde{\theta} = F_\theta. \tag{6c}$$

The forcing terms ($F_u$, $F_v$, $F_w$), $F_\phi$, and $F_\theta$, like the rhs of (3), are functions of the balanced solution and are given by the difference between the time tendency determined by substituting the balanced fields in (5) and the actual time tendency of the balanced solution. For example, the residual tendency for $u$ is

$$F_u = -\frac{\partial\tilde{u}}{\partial t} - \tilde{\mathbf{v}}\cdot\nabla\tilde{u} + f\tilde{v} - \frac{\partial\tilde{\phi}}{\partial x}. \tag{7}$$

Because the flow is nearly hydrostatic and incompressible, we also make the approximation that $F_w = F_\phi = 0$.

Since $R$ is small, $\tilde{\mathbf{v}}$ can be approximated by the geostrophic velocity $\tilde{\mathbf{v}}_g$ on the lhs of (6). We will examine the effects of this additional approximation in sections 4 and 5 by computing solutions both with $\tilde{\mathbf{v}} = \tilde{\mathbf{v}}_g$ and with $\tilde{\mathbf{v}} = \tilde{\mathbf{v}}_g + \tilde{\mathbf{v}}_a$, where $\tilde{\mathbf{v}}_a$ is the ageostrophic velocity. Expressions for $\tilde{\mathbf{v}}_g$ and $\tilde{\mathbf{v}}_a$ are given in the appendix.

Equations (5) are discretized and solved numerically, as outlined in SMPZ, using centered fourth-order differences for the advective terms and a time-split integration technique in which the terms associated with the propagation of linear acoustic waves are updated with a smaller time step. The linearized Eqs. (6) employ the same numerics; in fact, the linearized model is derived through the linearization of the discretized equations about the specified balanced solution. Both the nonlinear and linearized models also include fourth-order horizontal hyperdiffusion in the momentum and potential temperature equations, as well as damping of the three-dimensional divergence, as described in SMPZ.

We will take as the balanced solution the QG dipole vortex of Muraki and Snyder (2007), which was also used as initial conditions for the simulations of SMPZ. It has antisymmetric warm and cold anomalies at a horizontal boundary (in this case, the surface) and its purely geostrophic velocity decays smoothly away from the boundary owing to the uniform interior potential vorticity. The resulting forcing terms in (6) are specified in the appendix. As just noted, some experiments will also include the diagnosed ageostrophic velocity in $\tilde{\mathbf{v}}$ on the lhs of (6). Those experiments provide a measure of the sensitivity of the solution of (6) to the precise choice of the approximate balanced flow.

The QG dipole translates horizontally at a steady speed. In what follows, we will work in the frame of reference moving with the dipole, where the balanced solution is exactly steady.

Let the maximum wind speed of the QG dipole be denoted by $U$ and the radius of its region of surface $\theta$ anomaly be $L$. We will take $U$ and $L$ respectively as the characteristic velocity and length scales of the dipole. Results presented here will be based on $U = 10\ \text{m s}^{-1}$

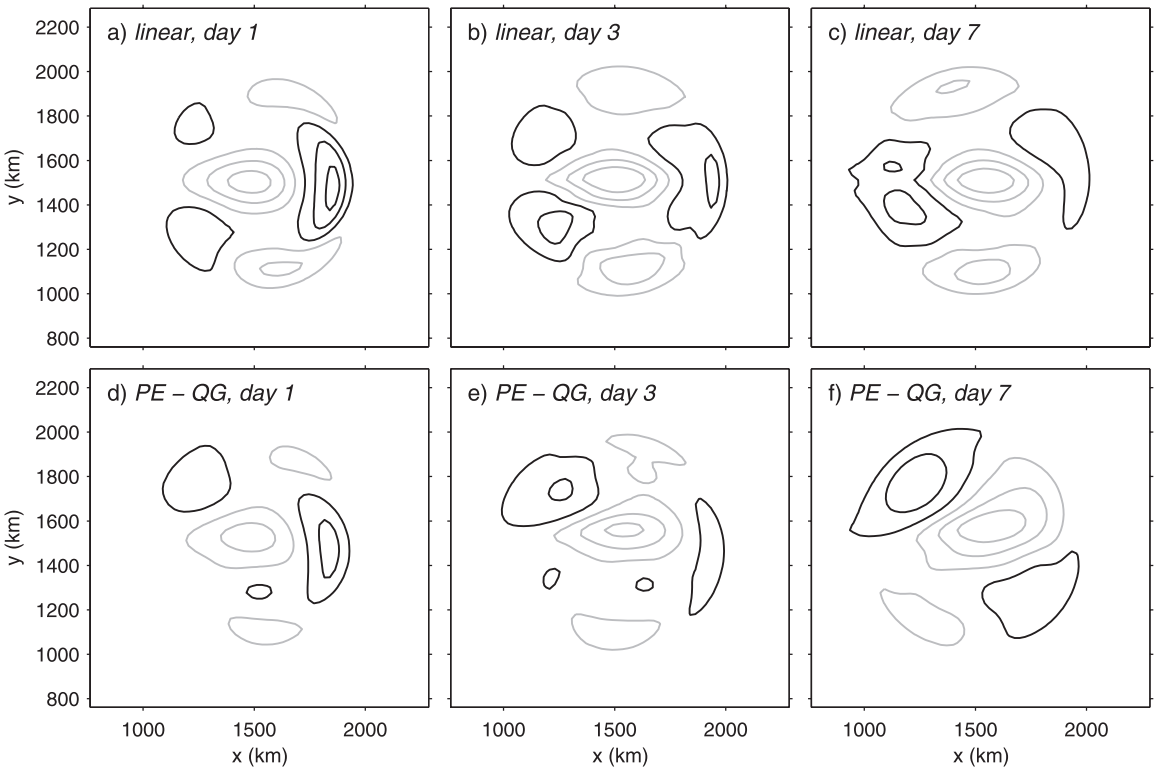


FIG. 1. Comparison of (top) the perturbations for $\theta$ at the lowest level above the surface as predicted by (3) with (bottom) the difference of the PE and QG dipole solutions. Days 1, 3, and 5 are shown. The contour internal is 0.3 K, with contours beginning at $\pm 0.15$ K and gray lines indicating negative values.

and $L = 500$ km, the same as the standard case considered in SMPZ. The dipole's translation speed is then approximately 1.1 m $s^{-1}$ and the Rossby number $R = 0.2$.

A crucial question is the accuracy of (6) in describing the evolution of differences between the QG solution and the full nonlinear solution of (5). The dipole evolves on the advective time scale $L/U$ or, equivalently, with time tendencies comparable to $U/L$. The QG equations give a leading-order approximation in $R$ to those tendencies. The difference between the PE and QG time tendencies will then have magnitude $RU/L$ and the relative error of the QG solution will be $O(1)$ for times $\Delta t$ such that $RU\Delta t/L = 1$. For $U = 10$ m $s^{-1}$ and $L = 500$ km, $\Delta t \approx 3$ days.

Thus, the solution of the forced linear solution should be an accurate approximation to the difference between the PE and QG solutions only for times less than a few $\Delta t$, or perhaps 10 days.

The time over which solutions of (6) are accurate can also be assessed through direct comparison with the difference between the PE and QG solutions. Figure 1 shows this comparison for $\theta$ at the lowest model level above the surface and after 1 day, 3 days, and 7 days of evolution. The $\theta$ perturbations have scales comparable to the dipole itself and the associated velocities (not shown) are approximately geostrophic. The forced linear solution is a useful approximation after 1 and 3 days but clearly begins to diverge by 7 days from the difference between PE and QG, consistent with the scaling arguments just given.

The difference between the PE and QG solutions at 7 days exhibits a tripolar pattern in $\theta$ that is tilted relative to the axis of the dipole. Comparison of the PE and QG dipoles (Fig. 2) shows that the differences arise from (i) a spreading of the cold anticyclone across the axis of the PE dipole, (ii) a slowing of the zonal propagation of the PE dipole, and (iii) a cyclonic rotation of the PE dipole. The latter behavior is consistent with the propagation of the PE dipole along a cyclonically curved path (see Fig. 2 of SMPZ). Together, these differences are an example of the secular growth of balanced corrections to the QG solution predicted by Warn et al. (1995).

In what follows, we will generally limit our use of the solutions to (3) to times less than $3\Delta t$ or about 10 days. The stationary inertia–gravity waves in the PE solution of SMPZ, in comparison, are clearly present by 10 days, although some transients also remain at that time. Thus, there is some overlap between the times at which

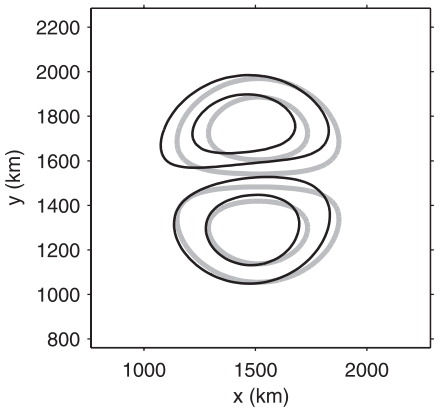


FIG. 2. Values of $\theta$ at the lowest level above the surface at day 7 for the PE dipole (black contours) and the QG dipole (gray). Contour interval is 1/5 the difference between the maximum and minimum $\theta$ for the QG dipole, or roughly 1.1 K.

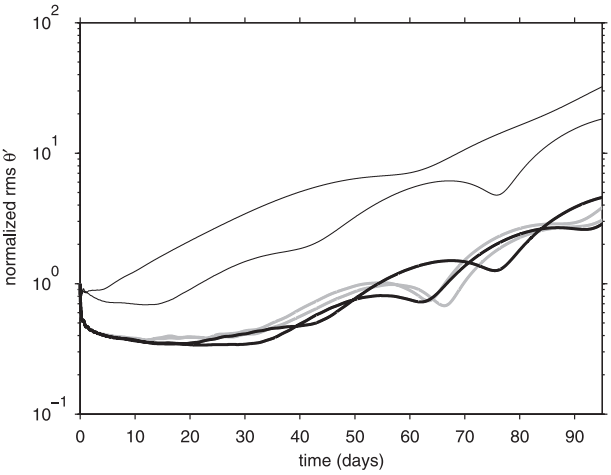


FIG. 3. Time series of rms $\theta'$ (i.e., the square root of the domain average of $\theta'^2$), normalized to have unit initial value. Results are shown for two different realizations of random white-noise initial perturbations in $\theta'$ (thick black lines), for the same two realizations but including $\mathbf{v}_a$ in the basic-state dipole (gray lines), and for two other initial conditions for $\theta'$ (thin lines): an axially symmetric monopole given by (8) and the meridional derivative of the monopole (which yields the largest $\theta'^2$ at each time).

stationary waves are present in the PE solutions and the time interval over which solutions of (6) are accurate.

## 4. Homogeneous solutions from random initial conditions

In this section, we consider solutions of (6) from random initial conditions and with the forcing terms on the rhs set to zero. This differs from a classical stability analysis in that we do not possess a steadily translating dipole solution for the PE.[2] Our approach provides information about the stability of the QG dipole to small perturbations under PE dynamics, but in a restricted sense. Solutions of (6), and thus any inferences about the dipole's stability, are valid only for times for which the QG dipole is a reasonable approximation to the evolution of the dipole under the PE, perhaps 10 days (for $U = 10$ m s$^{-1}$ and $L = 500$ km).

The initial conditions for the perturbations are given by white noise in $\theta'$ with unit variance for $0 < z < 3.25$ km. Initial perturbations for the velocity are zero for simplicity. Experiments with initial perturbations at all levels (not shown) exhibit very slow decay of the perturbations aloft but qualitatively similar behavior in the neighborhood of the basic-state dipole.

The evolution of the rms of $\theta'$ appears in Fig. 3 for two realizations of the initial perturbations (thick black lines). In either realization, the perturbation decays over the first 20 days. Since the decay is clearly partly an artifact of our choice of initial conditions that are not balanced and that have substantial power at the smallest, most heavily damped scales (Snyder et al. 2003), we extended the integrations to longer times, well beyond the nominal 10-day limit for the accuracy of the linear solutions, in order to isolate more rapidly growing disturbances. At later times, the perturbation amplitude grows slowly or oscillates, showing a net amplification by a factor of between 10 and 20 over the next 75 days. The timing of the oscillations in perturbation amplitude depends on the specific realization of the initial perturbation. The perturbation horizontal velocities behave similarly but for $w'$ the initial decay lasts for more than 30 days (not shown).

The perturbation growth is no stronger and its changes over time are qualitatively similar if the basic-state dipole includes ageostrophic velocities. The gray lines in Fig. 3 show the evolution of the rms of $\theta'$ for the same two realizations of the initial perturbations but including ageostrophic velocities in the basic state.

Although nonzero, these long-term amplifications are so small that we conclude that an instability is of doubtful relevance to inertia–gravity waves in the SMPZ simulations. Even an optimistic estimate from Fig. 3 would yield amplifications less than 1.5 over 10 days.

While these growing perturbations are of doubtful relevance to inertia–gravity waves in the SMPZ simulations, the mechanism by which they grow is of some

[2] Steadily translating dipoles (modons) have recently been obtained for the shallow-water equations (Kizner et al. 2008). The existence of such dipoles in continuously stratified fluid, where the phase speed of inertia–gravity waves no longer has a finite lower bound, is an open question.

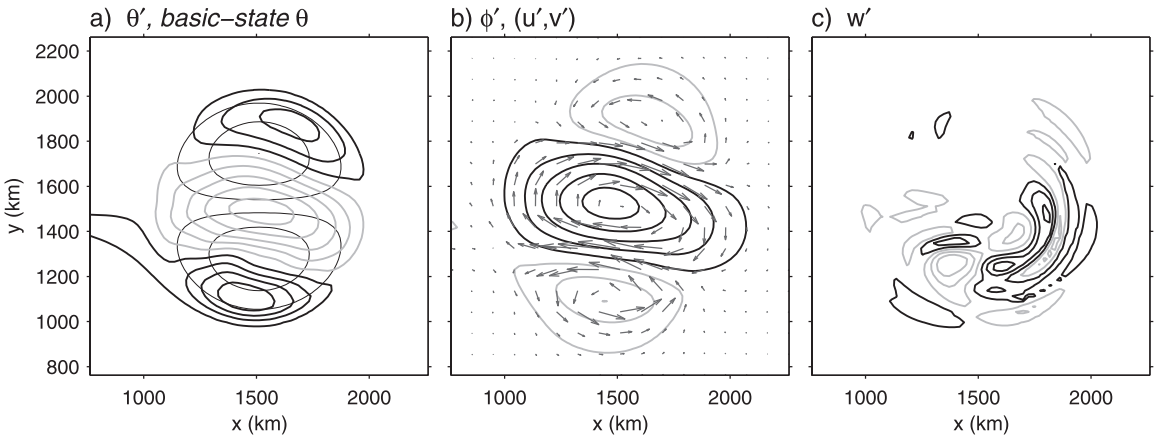


FIG. 4. Perturbation fields near the surface 55 days after the perturbation was initialized with random noise in $\theta'$ as described in the text: (a) $\theta'$ at $z = 125$ m (thick contours) overlaid on $\bar{\theta}$ (thin); (b) $\phi'$ (thick contours) and $\mathbf{v}'$ (vectors) at the same level; and (c) $w'$ at $z = 250$ m. Black and gray contours indicate positive and negative values, respectively, of the perturbation fields. Contour intervals are equal to $\frac{1}{5}$ of the maximum magnitude of field, with contours starting at $\pm\frac{1}{10}$, except for $w'$ where the interval is $\frac{3}{10}$ starting at $\pm 0.15$.

interest. We speculate that they are related to the balanced disturbances that grow algebraically on two-dimensional, barotropic dipoles (Snyder 1999). In that case, the initial perturbation is a monopolar vortex of uniform vorticity and the same radius as the basic-state dipole. The velocity associated with the disturbance vortex causes the dipole to rotate, leading to a dipolar difference from the basic-state dipole that grows linearly with $t$ in the small-amplitude limit, and the velocity associated with the growing dipolar disturbance in turn leads to a displacement of the basic-state dipole normal to its propagation direction, which grows as $t^2$.

To evaluate the relevance of such disturbances to our results, we have examined the evolution of two large-scale initial perturbations, the first monopolar and the second dipolar. The monopolar initial perturbation is given by

$$\theta'(x, y, z) = \exp\left\{\frac{-[(x - x_0)^2 + (y - y_0)^2 + \left(\frac{N^2}{f^2}\right)z^2]}{r^2}\right\}, \tag{8}$$

where $x_0 = y_0 = 1500$ km and the decay scale $r = 165$ km. Taking $\partial/\partial y$ of (8) gives the dipolar initial perturbation, which is antisymmetric across the $x$ axis. Again, the initial velocity perturbations are zero and the initial evolution of the perturbation exhibits considerable geostrophic adjustment.

Starting from either initial condition, $\theta'$ grows at roughly the same rate as in the simulations using white-noise initial conditions, though with little or no initial decay (Fig. 3). Thus, an initial perturbation similar to that considered by Snyder (1999), as well as other initial perturbations with scale similar to the dipole, efficiently excites the growing disturbance.

The structure of the growing perturbations provides further evidence. Although they do not converge to a fixed structure,[3] the growing perturbations that emerge have common qualitative characteristics. They have horizontal scale of $O(1000$ km), comparable to that of the basic-state dipole, and the horizontal velocity is approximately geostrophic as would be expected for perturbations of this scale. Like the basic-state dipole, the perturbations are surface trapped, so that regions of warm $\theta'$ are associated with negative $\phi'$ and cyclonic wind perturbations. These aspects of the perturbations' structure are illustrated in Fig. 4, which shows the near-surface structure of a perturbation that has evolved for 55 days from a specific realization of the random initial conditions. All these aspects of the perturbation structure are also consistent with what would be expected from a generalization of the results of Snyder (1999) to dipoles in stratified, rotating flow.

The details of the perturbation structure depend on the specific initial conditions. After looking at many realizations, we have observed cases in which, at some point in the perturbation's evolution, $\theta'$ is approximately dipolar (like $\bar{\theta}$), tripolar (like $\partial\bar{\theta}/\partial y$, as shown in Fig. 4), quadrupolar (like $\partial\bar{\theta}/\partial x$), or some superposition of these structures.

[3] The variability of the growth in Fig. 3 clearly indicates that the perturbations have not converged to a single dominant exponential mode, if one exists, even after 95 days. Consistent with this, the perturbation structure also does not converge but varies on the same time scale of 20–30 days, which is typical of the variations in growth.

Figure 4c shows the perturbation vertical velocity. Like $w$ in the nonlinear simulations of SMPZ, $w'$ exhibits a strong signature of inertia–gravity waves with horizontal scales of $O(100$ km). The wave crests form long curved bands near the leading edge of the basic-state dipole. This is a clear indication that the nonconstant coefficients of the lhs linear operator in (3) play a significant role in determining the spatial structure of the wave response.

## 5. Solutions forced by the residual tendencies

Because an instability of the dipole appears unlikely to explain the inertia–gravity waves found in the SMPZ simulations, we turn next to the solution of (6) starting from zero initial conditions and forced by the residual tendencies from the QG dipole. This solution approximates the evolution of the difference between the QG dipole and the PE solution initialized from the QG dipole. As discussed in section 3, the approximation is reasonable for $\theta'$ at early times but breaks down after a few advective time scales, or about 10 days in the present case.

The volume-averaged amplitude of the forced solution appears in Fig. 5 as a function of time. The vertical velocity perturbation peaks in the first hour and then decays steadily until reaching a roughly constant value between days 10 and 20. The rms of the other variables ($u'$, $v'$, and $\theta'$) increases rapidly over the first day and then varies more slowly until roughly day 10, at which point the amplitude begins a steady increase at roughly the rate seen at long times in the unforced simulations (Fig. 3). The growth at long times (beyond 10 days) is qualitatively consistent with that found in the homogeneous solutions and appears to arise from the excitation of the growing disturbances by the forcing. As for the homogeneous solutions, we do not believe that these long-time growing solutions are relevant to the dipole.

The rapid increase at early times is associated with a transient adjustment to the forcing. Animations of $w'$ over the first 1–2 days clearly reveal gravity waves propagating away from the dipole. This is the linearized model's version of the geostrophic adjustment that occurs when the PE are initialized with the QG dipole.

The inertia–gravity waves emitted continuously within the dipole are also evident in the forced solutions. Figures 6a–c show $w'$ at the lowest model level for days 3, 5, and 10. Like the difference between the PE and QG dipoles (Figs. 6d–f), $w'$ from the forced solution exhibits a pattern of alternating upward and downward motion whose horizontal wavelength, at $O(100$ km), is short compared to the dipole radius and whose phase lines curve along the leading edge of dipole. Overall there is striking qualitative agreement in the patterns of vertical motion from the two solutions, especially near the leading edge of the dipole and after day 5. In addition, the spatial structure of $w'$, like that of the difference between the PE and QG $w$, varies little from day 5 to day 10.

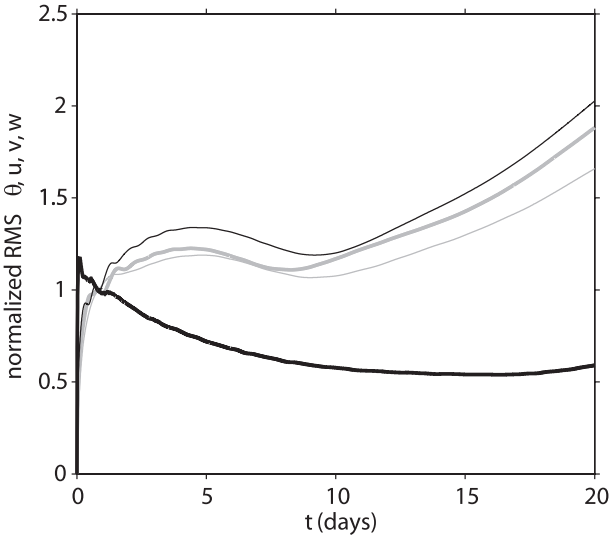


FIG. 5. Time series of rms $\theta'$, $u'$, $v'$, and $w'$ (thin black, thin gray, thick gray, and thick black, respectively) for the forced solution of (6) starting from zero initial conditions. Each variable is normalized to have unit rms value at day 1.

Arguably, the agreement between the upper and lower panels of Fig. 6 is better at days 5 and 10 than at day 3. The forced linear simulation thus appears to capture the steady response better than the transient waves from the initial adjustment. The reasons for this are not clear to us, although the transient waves, whose amplitude is substantially larger (see our Fig. 5, as well as Fig. 1 of SMPZ), may be more nonlinear and therefore subject to larger errors in the linearized simulations.

The qualitative agreement between the forced, linear $w'$ and the PE-minus-QG difference can also be seen in vertical cross sections along the dipole axis ($y = 1500$ km), which appear in Fig. 7 for day 10. The dominant features of both solutions are a couplet of downward and upward motion near the center of the dipole ($x \approx 1500$ km) followed by an inertia–gravity wave packet near the leading edge of the dipole that has phase lines tilting toward the west with height. As discussed in detail in SMPZ, the phase tilts within the wave packet are consistent with upward group velocity, since the local horizontal flow is to the east (toward the leading edge of the dipole) and the wave frequency is approximately zero.

Thus, the picture that emerges is that the forcing by the residual tendencies, which is strongly confined at low levels (see the appendix), generates waves with upward group velocity. As with mountain waves, the stationary forcing together with flow relative to the forcing, which

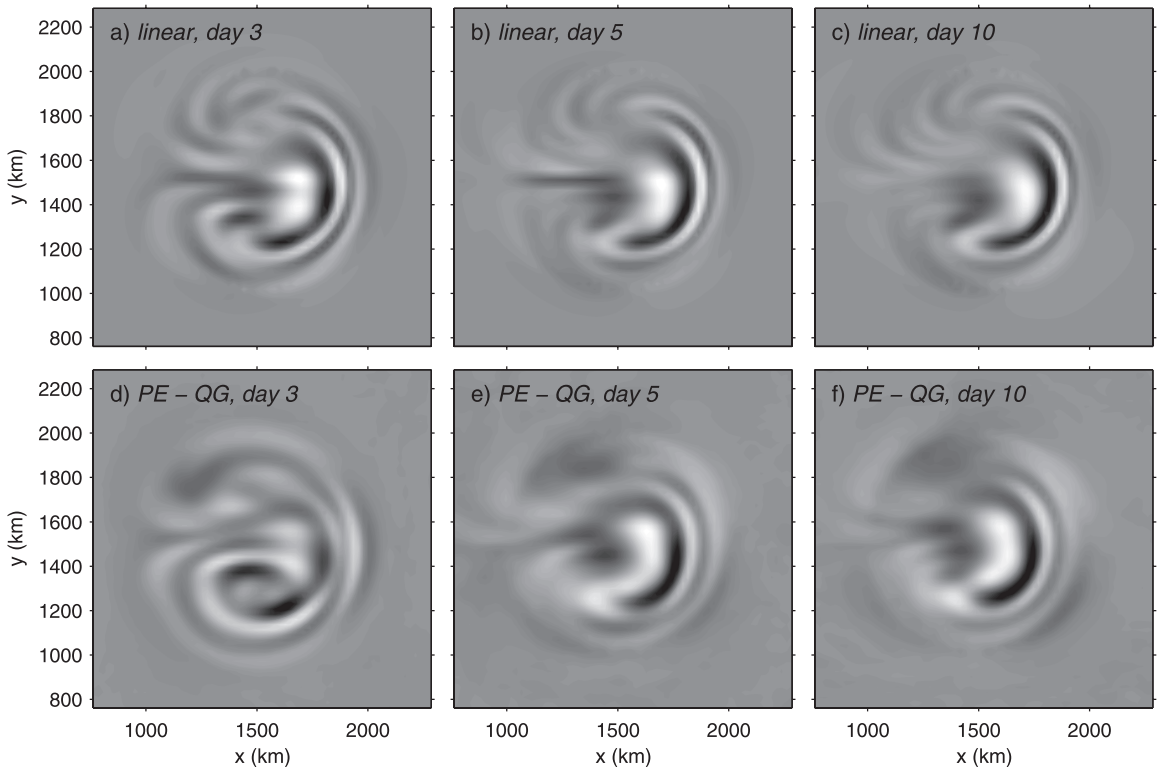


FIG. 6. As in Fig. 1, but for days 3, 5, and 10 and comparing $w'(x, y)$ at the lowest level above the surface from (a)–(c) the forced, linear solutions of (6) and from (d)–(f) the difference of the PE and QG dipole solutions. The gray shading varies linearly between white at 0.9 times the maximum $|w'|$ in each panel and black at $-0.9$ times that maximum. The maximum $|w'|$ is 0.20, 0.17, 0.15, 0.16, 0.08, and 0.08 cm $s^{-1}$ in (a)–(f), respectively.

is provided by the jet along the dipole's axis, produces a stationary response.

Some disagreements between the two solutions are also apparent. The dominant features in the forced linear solution lie about 100 km to the east of their counterparts in the PE solution. This shift is caused, at least in part, by the comparable westward shift (and cyclonic rotation) of the PE dipole relative the QG dipole, which can be seen in Fig. 2. Another disagreement lies in the relatively stronger variations in $w$ above 1.5 km. Those variations are largely remnants of the initial geostrophic adjustment and can be seen propagating slowly upward in time sequences of vertical cross sections (not shown).

Figure 8 provides a more detailed view of the spatial structure and time dependence of the vertical velocity, showing $w'(x)$ from the forced linear solution at the lowest

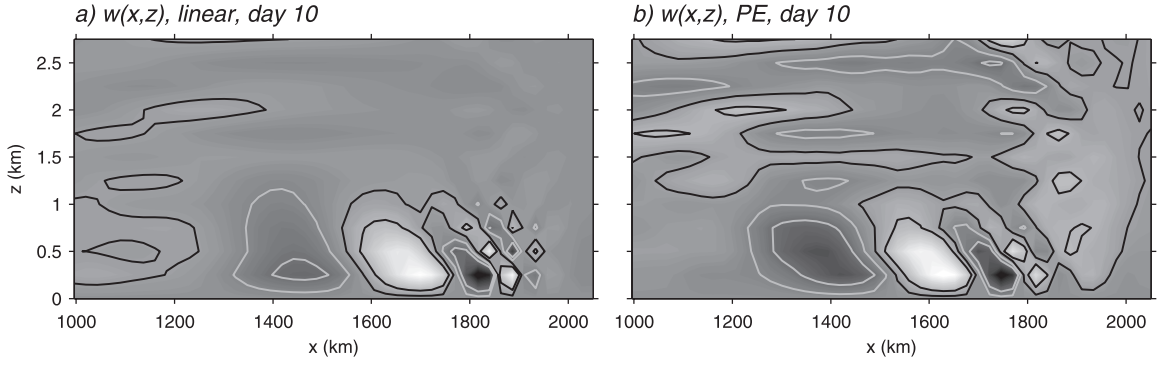


FIG. 7. Comparison at $y = 1500$ km and day 10 of (a) $w'(x, z)$ from the forced, linear solution of (6) and (b) the difference in $w(x, z)$ between the PE and QG dipole. The gray shading varies linearly between white at 0.9 times the maximum $|w'|$ in each panel and black at $-0.9$ times that maximum and contours are shown at $\pm 0.1$ and $\pm 0.3$ times the maximum $|w'|$; gray contours indicate negative values.

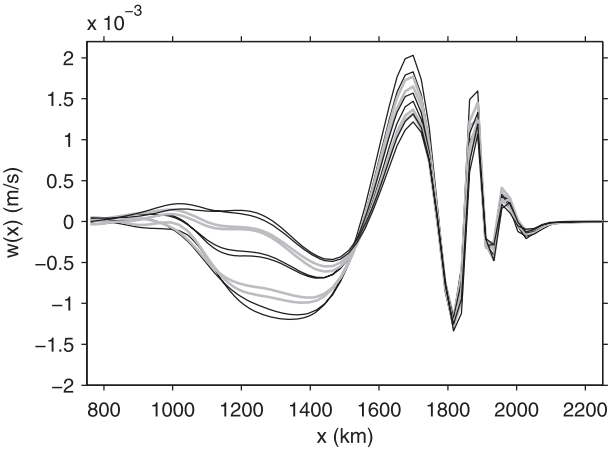


FIG. 8. Perturbation vertical velocity $w'(x)$ from the forced, linear solution at the lowest model level and $y = 1500$ km at times beginning at day 5 and extending to day 9.5 every 12 h (days 5 and 5.5, black lines; pairs of lines from subsequent days alternate between gray and black). In the interval 1200 km $< x <$ 1700 km, the amplitude of $w'$ decreases nearly monotonically with time.

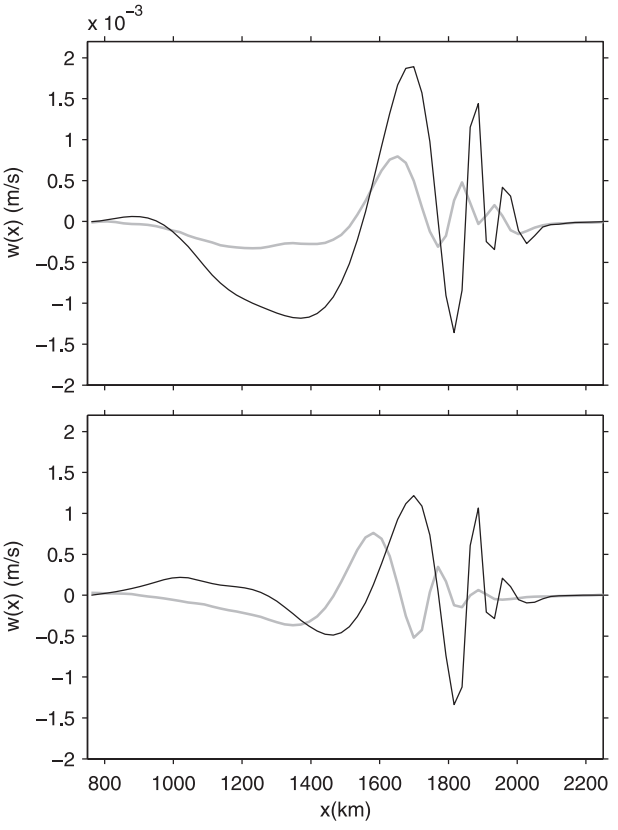


FIG. 9. As in Fig. 8, but comparing the forced, linear $w'(x)$ (black lines) with the difference in $w(x)$ between the PE and QG dipoles (gray) at days (top) 5 and (bottom) 10.

model level and along the axis of the dipole ($y = 1500$ km) every 12 h from day 5 to day 10. Toward the leading edge of the dipole, the wavelength shrinks as one moves eastward and, for $x > 1700$ km, the waves are nearly steady; both these characteristics are shared with the waves in the SMPZ simulations. Near the center of the dipole, the descent–ascent couplet undergoes substantially more time dependence. Between days 5 and 10, its amplitude decreases by more than a factor of 2 and the horizontal extent of the descending air contracts considerably.

Figure 9 compares $w'(x)$ from the forced, linear solution with the PE-minus-QG difference. At day 5, $w'$ is roughly twice as large as the PE-minus-QG difference, although the agreement is somewhat better by day 10 owing to the decrease of $w'$. The phase shift between the two solutions, already noted in Fig. 7, is also obvious and increases from day 5 to day 10 as the PE dipole lags farther behind the position of the QG dipole.

Instead of the QG dipole, solutions to any of a number of other balanced equation sets could also be employed as approximations to the PE dipole. These other balanced solutions would differ from the QG dipole by terms of $O(R)$ relative to the leading-order, QG dynamics. We next examine the sensitivity of the forced solution to such $O(R)$ changes in either the balanced winds $\tilde{\mathbf{v}}$ or in the forcing itself.

Neglecting the ageostrophic advection of ageostrophic wind, which is $O(R)$ compared to the full forcing, in $F_u$ and $F_v$ results in changes of roughly 10% in their magnitude (see the appendix).

The resulting forced solutions of (6) have correspondingly small changes (not shown); the pattern, magnitude, and evolution of $w'$, for example, are quantitatively close to the solutions shown in Figs. 6–8 based on the full forcing. Thus, the forced solutions are not sensitive to those details of the forcing.

The forced solutions are, however, sensitive to including ageostrophic velocities in the basic-state dipole [that is, if $\tilde{\mathbf{v}}$ on the lhs of (6) includes ageostrophic velocities]. The perturbation vertical velocity $w'$ for this solution appears in Fig. 10 at the same times shown in Fig. 6. The inertia–gravity waves are now much stronger within the anticyclone than the cyclone and form a spiral pattern concentrated within the anticyclone rather than arcs toward the leading edge of the dipole. The pattern of $w'$ again becomes nearly steady by day 5 but, unlike the case with a purely geostrophic basic-state dipole, its magnitude grows steadily.

The ageostrophic flow has the form of anticyclonic gyres to either side of the jet along the dipole axis. Including the ageostrophic velocity in $\tilde{\mathbf{v}}$ therefore leads to a shift of jet toward the anticyclone, along with an enhancement of the anticyclonic vorticity (from $-0.7f$ to $-0.9f$) and a reduction of the cyclonic vorticity (from $0.7f$ to $0.5f$). Both these differences are qualitatively

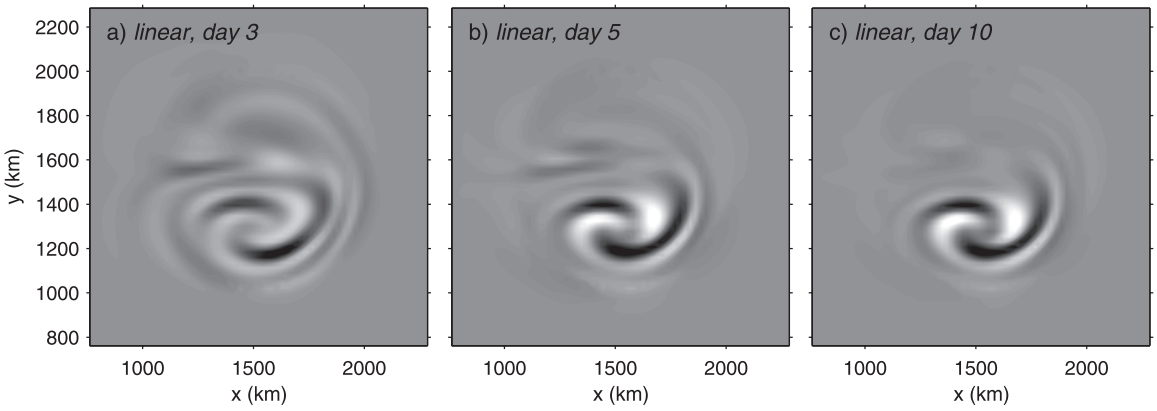


FIG. 10. As in Fig. 6, but showing the forced, linear $w'(x, y)$ when $\tilde{\mathbf{v}}_a$ is included in the basic state dipole. [More precisely, the advective terms in (6) employ $\tilde{\mathbf{v}} = \tilde{\mathbf{v}}_g + \tilde{\mathbf{v}}_a$ rather than $\tilde{\mathbf{v}} = \tilde{\mathbf{v}}_g$.] The maximum $|w'|$ is 0.28, 0.38, and 0.54 cm s$^{-1}$ in panels (a)–(c), respectively.

consistent with the concentration of waves in the anticyclone. Wang et al. (2009) use ray tracing to demonstrate a similar effect from shifting the jet toward the anticyclone and the local enhancements of anticyclonic vorticity tend to trap small-scale, near-inertial waves by modifying their dispersion.

As noted above, the ageostrophic velocities are formally an $O(R)$ correction to the QG flow. One might then expect that including them in $\tilde{\mathbf{v}}$ on the lhs of (6) would improve the correspondence between $w'$ and the PE-minus-QG differences. In fact, $R$ is not small enough to insure that additional terms improve the approximation: including $\mathbf{v}_a$ makes the asymmetry between cyclonic and anticyclonic vorticity substantially too large and drives the absolute vorticity (and PV) in the anticyclone almost to zero. Wave propagation thus becomes unrealistically enhanced in the anticyclone.

## 6. Summary and conclusions

This paper has investigated the generation mechanism for the stationary inertia–gravity waves embedded within a larger-scale dipole vortex, as seen in the numerical simulations of SMPZ and others.

Because the waves have small amplitude in horizontal velocity and potential temperature relative to the dipole, we consider the numerical simulations to be the sum of an approximate balanced solution, given by the QG dipole of Muraki and Snyder (2007), and a small deviation that may include waves as well as balanced corrections to the QG dipole. To leading order in their amplitude, the deviations satisfy linear equations, based on linearization about the QG dipole and forced by the residual tendency of the QG dipole (i.e., the difference between the time tendency of the QG solution and that of the full primitive equations initialized with the QG fields). The linear equations accommodate two possible wave-generation mechanisms: either an instability of the dipole, which would appear as a growing homogeneous solution, or forcing of inertia–gravity waves by the residual tendencies.

We considered, but dismiss based on our results, the possibility that the waves are associated with an instability of the balanced dipole. While numerical solutions of the homogeneous linear equations do reveal growing disturbances, they are nearly geostrophic, have length scales comparable to the dipole itself, and grow too slowly to explain the stationary waves in the full nonlinear simulations of SMPZ. Instead, these growing disturbances represent balanced corrections to the QG dipole, which are to be expected since the dipole in the nonlinear simulations propagates more slowly than the QG dipole and along a slightly curved path.

The linear solutions forced by the residual tendencies, in contrast, yield excellent qualitative agreement with nonlinear simulations for the packet of inertia–gravity waves at the leading edge of the dipole, correctly predicting the scale and pattern of the wave crests and the fact that they are stationary relative to the dipole and have nearly steady amplitude. Quantitatively, the forced linear solution overestimates the amplitude of the waves by roughly a factor of 2.

Scale analysis of the inertia–gravity wave dispersion relation indicates the characteristics of the waves to be expected in the forced linear solution. It is crucial to allow for the presence of the ambient flow associated with the QG dipole and to consider the intrinsic frequency of the waves. (The QG flow is also important for the advection and refraction of waves after they are forced.) Consistent with the wave characteristics in the SMPZ simulations, the dispersion relation predicts that the waves should be small scale compared to the balanced

flow, should be approximately stationary in the frame of reference moving with the dipole, and should have near-inertial intrinsic frequency.

Thus, there is strong evidence that inertia–gravity waves in the SMPZ simulations are, to a first approximation, a linear forced response to the presence of the dipole. A more conclusive demonstration will require better quantitative agreement between the linear solutions and the waves present in the nonlinear simulation. We believe this can be achieved through the use of a balanced approximation to the dipole that is more accurate than QG, since the linear solutions presented here depend significantly on the details of the balanced solutions. Decreasing $R$ is another possible approach, but one that will increase the scale separation between the dipole and the waves and thus increase the computational demands.

This mechanism for wave generation is analogous to that of Lighthill (1952) and Ford et al. (2000) in that the waves can be computed as a linear response to a forcing that is a known function of the balanced solution. The waves generated by the dipole, however, are smaller scale than the dipole and have inverse frequencies comparable to its advective time scale. Although a rigorous theory does not yet exist, extending the Lighthill–Ford arguments to small $R$ is expected to yield generation of fast waves with spatial scale comparable to the balanced motion (e.g., Saujani and Shepherd 2002), precisely the opposite relation of scales between the waves and balanced flow. The dipole can generate small-scale waves because fluid parcels within the dipole move relative to the forcing, which allows a wave response at those wavenumbers $k$ large enough that the intrinsic frequency is larger than $f$. This emphasizes both the role of a spatially varying flow in wave generation and the association of this mode of wave generation with the high-wavenumber tail of the balanced motion's spatial spectrum rather than the high-frequency tail of the temporal spectrum identified in previous studies (Errico 1982; Warn 1997; Saujani and Shepherd 2002; Vanneste 2008). Wave generation in the dipole resembles the production of stationary waves by flow over orography rather than by an oscillator in a fluid at rest.

Of course, most balanced flows have nontrivial time dependence and their wave generation will fit neither view precisely. Idealized studies of frontogenesis, for example, exhibit generation of waves that are stationary relative to the frontal circulation (Snyder et al. 1993) as well as wave generation through time variation of the frontogenesis (Reeder and Griffiths 1996). We note, however, that the most prominent inertia–gravity waves generated within synoptic-scale baroclinic systems appear to be generated in a manner similar to that described here, as the waves are approximately stationary with respect to the parent baroclinic system (Plougonven and Snyder 2007).

*Acknowledgments.* This work was supported at NCAR in part by Grant CMG-0327582 from the National Science Foundation.

## APPENDIX

### $F_u$, $F_v$, and $F_\theta$ for QG Dipole

The residual tendencies $F_u$, $F_v$, and $F_\theta$ are differences between the time tendency of the balanced solution and the tendency that would be obtained by substituting the balanced solution in the PE, following (3) and as expressed for $F_u$ in (7). These residuals are easily calculated for the QG dipole.

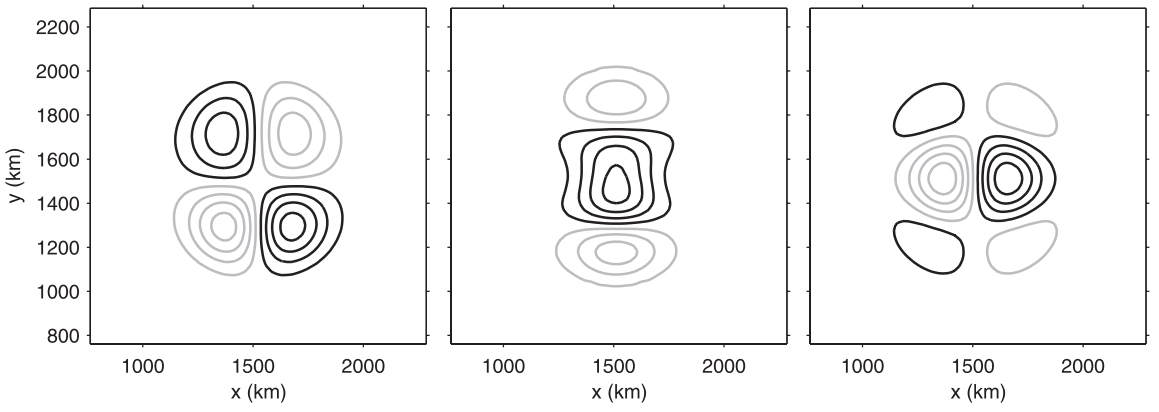


FIG. A1. Residual tendencies (left) $F_u$, (center) $F_v$, and (right) $F_\theta$ for the QG dipole of Muraki and Snyder (2007). Black (gray) contours indicate positive (negative) values. Contour values are $\pm 1, 3, 5$, and $7 \times 10^{-6}$ m s$^{-2}$ for the momentum forcings $F_u$ and $F_v$, and $\pm 0.2, 0.6, 1$, and $1.4 \times 10^{-6}$ K s$^{-1}$ for $F_\theta$.

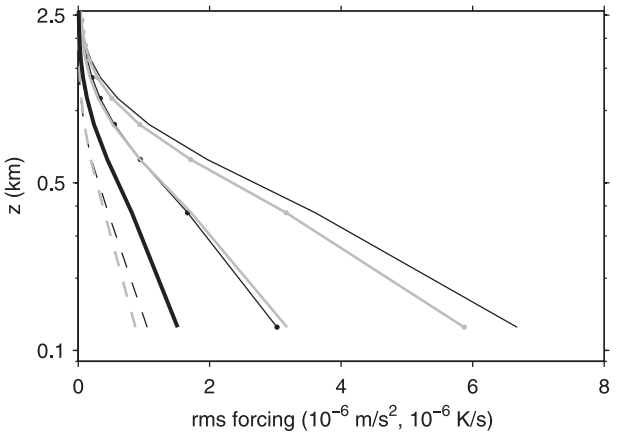


FIG. A2. Variation with height of square root of area-mean squared contributions to the residual tendencies: $\tilde{\mathbf{v}}_g \cdot \nabla \tilde{u}_a$ (black lines, dots at data points), $\tilde{\mathbf{v}}_a \cdot \nabla \tilde{u}_g$ (black, no dots), $\tilde{\mathbf{v}}_a \cdot \nabla \tilde{u}_a$ (dashed black), $\tilde{\mathbf{v}}_g \cdot \nabla \tilde{v}_a$ (gray, with dots), $\tilde{\mathbf{v}}_a \cdot \nabla \tilde{v}_g$ (gray, no dots), $\tilde{\mathbf{v}}_a \cdot \nabla \tilde{v}_a$ (dashed gray), and $\tilde{\mathbf{v}}_a \cdot \nabla \tilde{\theta}$ (thick black). Note the logarithmic scale of the $z$ axis.

Denoting the QG solution by tildes, all fields can be derived from $\tilde{\phi}$. Let us define $\tilde{\mathbf{v}} = \tilde{\mathbf{v}}_g + \tilde{\mathbf{v}}_a$, where the geostrophic velocity is given by $\tilde{\mathbf{v}}_g = f^{-1}\mathbf{k} \times \nabla\tilde{\phi}$ and the ageostrophic velocity $\tilde{\mathbf{v}}_a$ can be diagnosed from the QG momentum and potential-temperature equations,

$$\tilde{u}_a = -f^{-1}\left(\frac{\partial}{\partial t} + \tilde{\mathbf{v}}_g \cdot \nabla\right)\tilde{v}_g, \tag{A1a}$$

$$\tilde{v}_a = f^{-1}\left(\frac{\partial}{\partial t} + \tilde{\mathbf{v}}_g \cdot \nabla\right)\tilde{u}_g, \quad \text{and} \tag{A1b}$$

$$\tilde{w} = -\left(\frac{g}{\theta_0}\right)N^{-2}\left(\frac{\partial}{\partial t} + \tilde{\mathbf{v}}_g \cdot \nabla\right)\tilde{\theta}. \tag{A1c}$$

Substituting the QG fields into the formulas for the residual tendencies [namely (7) and its counterparts for $F_v$ and $F_\theta$] then gives

$$F_u = -\tilde{\mathbf{v}}_a \cdot \nabla\tilde{u} - \tilde{\mathbf{v}}_g \cdot \nabla\tilde{u}_a,$$

$$F_v = -\tilde{\mathbf{v}}_a \cdot \nabla\tilde{v} - \tilde{\mathbf{v}}_g \cdot \nabla\tilde{v}_a, \quad \text{and}$$

$$F_\theta = -\tilde{\mathbf{v}}_a \cdot \nabla\tilde{\theta},$$

where we have used (A1) and the fact the QG tendencies are zero in the frame moving with the dipole.

Figure A1 illustrates the horizontal structure of each residual tendency. Both $F_v$ and $F_\theta$ have maxima near the center of the dipole and along the axis of the surface jet. Owing to their dependence on derivatives and products of the QG fields, the spatial scale of the residual tendencies is 200–300 km, somewhat smaller than that of the dipole itself.

Because the QG dipole has uniform (pseudo)potential vorticity, all the fields except $w'$ decay upward from the surface. Consistent with this, the residual tendencies also decay rapidly with height (Fig. A2) and have negligible magnitude above $z = 2$ km. The relative magnitudes of the various terms in $F_u$ and $F_v$ are also as would be expected, given that $R$ is small: $\tilde{\mathbf{v}}_g \cdot \nabla\tilde{\mathbf{v}}_a$ is comparable to $\tilde{\mathbf{v}}_a \cdot \nabla\tilde{\mathbf{v}}_g$, while $\tilde{\mathbf{v}}_a \cdot \nabla\tilde{\mathbf{v}}_a$ is small compared to either.

## REFERENCES


Errico, R. M., 1982: Normal mode initialization and the generation of gravity waves by quasigeostrophic forcing. *J. Atmos. Sci.,* **39,** 573–586.

Ford, R., 1994a: The instability of an axisymmetric vortex with monotonic potential vorticity in rotating shallow water. *J. Fluid Mech.,* **280,** 303–334.

——, 1994b: The response of a rotating ellipse of uniform potential vorticity to gravity wave radiation. *Phys. Fluids,* **6A,** 3694–3704.

——, M. E. McIntyre, and W. A. Norton, 2000: Balance and the slow quasimanifold: Some explicit results. *J. Atmos. Sci.,* **57,** 1236–1254.

Guest, F. M., M. J. Reeder, C. J. Marks, and D. J. Karoly, 2000: Inertia–gravity waves observed in the lower stratosphere over Macquarie Island. *J. Atmos. Sci.,* **57,** 737–752.

Kizner, Z., G. Reznik, B. Fridman, R. Khvoles, and J. McWilliams, 2008: Shallow-water modons on the *f*-plane. *J. Fluid Mech.,* **603,** 305–329.

Ley, B., and W. R. Peltier, 1978: Wave generation and frontal collapse. *J. Atmos. Sci.,* **35,** 3–17.

Lighthill, M. J., 1952: On sound generated aerodynamically. I. General theory. *Proc. Roy. Soc. London,* **211A,** 564–587.

McIntyre, M., 2009: Spontaneous imbalance and hybrid vortex-gravity structures. *J. Atmos. Sci.,* **66,** 1315–1326.

Medvedev, A. S., and N. M. Gavrilov, 1995: The nonlinear mechanism of gravity wave generation by meteorological motions in the atmosphere. *J. Atmos. Terr. Phys.,* **57,** 1221–1231.

Muraki, D. M., and C. Snyder, 2007: Vortex dipoles for surface quasigeostrophic models. *J. Atmos. Sci.,* **64,** 2961–2967.

Plougonven, R., and C. Snyder, 2005: Gravity waves excited by jets: Propagation versus generation. *Geophys. Res. Lett.,* **32,** L18802, doi:10.1029/2005GL023730.

——, and ——, 2007: Inertia–gravity waves spontaneously generated by jets and fronts. Part I: Different baroclinic life cycles. *J. Atmos. Sci.,* **64,** 2502–2520.

——, and F. Zhang, 2007: On the forcing of inertia–gravity waves by synoptic-scale flows. *J. Atmos. Sci.,* **64,** 1737–1742.

——, H. Teitelbaum, and V. Zeitlin, 2003: Inertia gravity wave generation by the tropospheric midlatitude jet as given by the Fronts and Atlantic Storm-Track Experiment radio soundings. *J. Geophys. Res.,* **108,** 4686, doi:10.1029/2003JD003535.

——, D. J. Muraki, and C. Snyder, 2005: A baroclinic instability that couples balanced motions and gravity waves. *J. Atmos. Sci.,* **62,** 1545–1559.

Reeder, M. J., and M. Griffiths, 1996: Stratospheric inertia-gravity waves generated in a numerical model of frontogenesis. II: Wave sources, generation mechanisms and momentum fluxes. *Quart. J. Roy. Meteor. Soc.,* **122,** 1175–1195.

Sakai, S., 1989: Rossby–Kelvin instability: A new type of ageostrophic instability caused by a resonance between Rossby waves and gravity waves. *J. Fluid Mech.,* **202,** 149–176.

Saujani, S., and T. G. Shepherd, 2002: Comments on ''Balance and the slow quasimanifold: Some explicit results.'' *J. Atmos. Sci.,* **59,** 2874–2877.

Snyder, C., 1999: Error growth in flows with finite-amplitude waves or other coherent structures. *J. Atmos. Sci.,* **56,** 500–506.

——, W. Skamarock, and R. Rotunno, 1993: Frontal dynamics near and following frontal collapse. *J. Atmos. Sci.,* **50,** 3194–3212.

——, T. M. Hamill, and S. Trier, 2003: Linear evolution of forecast error covariances in a quasigeostrophic model. *Mon. Wea. Rev.,* **131,** 189–205.

——, D. J. Muraki, R. Plougonven, and F. Zhang, 2007: Inertia–gravity waves generated within a dipole vortex. *J. Atmos. Sci.,* **64,** 4417–4431.

Vanneste, J., 2008: Exponential smallness of inertia–gravity wave generation at small Rossby number. *J. Atmos. Sci.,* **65,** 1622–1637.

——, and I. Yavneh, 2004: Exponentially small inertia–gravity waves and the breakdown of quasigeostrophic balance. *J. Atmos. Sci.,* **61,** 211–223.

Viúdez, A., 2007: The origin of the stationary frontal wave packet spontaneously generated in rotating stratified vortex dipoles. *J. Fluid Mech.,* **593,** 359–383.

——, 2008: The stationary frontal wave packet spontaneously generated in mesoscale dipoles. *J. Phys. Oceanogr.,* **38,** 243–256.

Wang, S., F. Zhang, and C. Snyder, 2009: Generation and propagation of inertia–gravity waves from vortex dipoles and jets. *J. Atmos. Sci.,* **66,** 1294–1314.

Warn, T., 1997: Nonlinear balance and quasi-geostrophic sets. *Atmos.–Ocean,* **35,** 135–145.

——, O. Bokhove, T. G. Shepherd, and G. K. Vallis, 1995: Rossby number expansions, slaving principles, and balance dynamics. *Quart. J. Roy. Meteor. Soc.,* **121,** 723–739.

Zhang, F., 2004: Generation of mesoscale gravity waves in upper-tropospheric jet-front systems. *J. Atmos. Sci.,* **61,** 440–457.